PHILOSOPHICAL TRANSACTIONS A

royalsocietypublishing.org/journal/rsta

Research

Cite this article: Hoffman MJ, Cherry EM. 2020 Sensitivity of a data-assimilation system for reconstructing three-dimensional cardiac electrical dynamics. *Phil. Trans. R. Soc. A* **378**: 20190388.
http://dx.doi.org/10.1098/rsta.2019.0388

Accepted: 25 February 2020

One contribution of 16 to a theme issue 'Uncertainty quantification in cardiac and cardiovascular modelling and simulation'.

Subject Areas:
biomathematics, mathematical modelling, computer modelling and simulation

Keywords:
state reconstruction, scroll waves, arrhythmia, model error

Author for correspondence:
Elizabeth M. Cherry
e-mail: elizabeth.cherry@gatech.edu

Sensitivity of a data-assimilation system for reconstructing three-dimensional cardiac electrical dynamics

Matthew J. Hoffman[1] and Elizabeth M. Cherry[2]

[1]School of Mathematical Sciences, Rochester Institute of Technology, Rochester, NY 14623, USA
[2]School of Computational Science and Engineering, Atlanta, GA 30332, USA

EMC, 0000-0001-5194-9572

Modelling of cardiac electrical behaviour has led to important mechanistic insights, but important challenges, including uncertainty in model formulations and parameter values, make it difficult to obtain quantitatively accurate results. An alternative approach is combining models with observations from experiments to produce a data-informed reconstruction of system states over time. Here, we extend our earlier data-assimilation studies using an ensemble Kalman filter to reconstruct a three-dimensional time series of states with complex spatio-temporal dynamics using only surface observations of voltage. We consider the effects of several algorithmic and model parameters on the accuracy of reconstructions of known scroll-wave truth states using synthetic observations. In particular, we study the algorithm's sensitivity to parameters governing different parts of the process and its robustness to several model-error conditions. We find that the algorithm can achieve an acceptable level of error in many cases, with the weakest performance occurring for model-error cases and more extreme parameter regimes with more complex dynamics. Analysis of the poorest-performing cases indicates an initial decrease in error followed by an increase when the ensemble spread is reduced. Our results suggest avenues for further improvement through increasing ensemble spread by incorporating additive inflation or using a parameter or multi-model ensemble.

THE ROYAL SOCIETY PUBLISHING

This article is part of the theme issue 'Uncertainty quantification in cardiac and cardiovascular modelling and simulation'.

1. Introduction

During arrhythmic states like ventricular fibrillation, the heart can experience complicated spatio-temporal states, including one or more re-entrant scroll waves of electrical activity [1–3]. Understanding these complicated dynamics is compounded by the difficulty in observing all the information that typically would be desired, often multiple state variables at high spatio-temporal resolution. In particular, *in vitro* experiments using high-resolution optical mapping [4–7] typically are limited to recordings of voltage and possibly intracellular calcium from only the exposed surfaces of the tissue, with only limited ability for observations in the tissue interior [8].

Mathematical and computational models provide another useful tool for studying cardiac dynamics and have been useful for gaining insights into many phenomena, including alternans [9–17], the stability of spiral and scroll waves [18–24], and control [25–33]. However, although the models often can be tuned to match a small set of tissue-level biomarkers (such as action potential duration at one frequency or re-entrant wave frequency), they typically do not produce detailed state estimates with sufficient quantitative accuracy to reproduce experimental or clinical observations. Several factors contribute to this lack of accuracy, and although biological heterogeneity and variability should not be overlooked, significant modelling issues including uncertainty in the values of model parameters and in the model equations themselves as well as difficulty in calibrating the models are critical impediments. A number of previous efforts have focused on improving the accuracy and reliability of cardiac models in various ways. Such efforts include making improvements to the models themselves, such as through better methods for parameter estimation [34–38] or through the development and use of models with fewer parameters [19,39–41] to reduce issues of identifiability [42], by seeking to improve predictions through the use of a population of models [43–48], or by tracking uncertainty in aspects of the model and propagating that uncertainty forward to predictions [49,50]. These approaches may lead to improvements in the accuracy of models and their predictions.

Here, we seek to use models for a somewhat different purpose: to create a high-resolution reconstruction of the dynamics of an experiment where direct observations are sparse in space and in time as well as in model space, in the sense that typically only one or two variables can be observed directly. In this setting, the model is used to provide an initial estimate of the state, but that estimate is updated when observations are available. The relative weights of the model estimate and the observations during the assimilation process are changed dynamically depending on the level of uncertainty in both.

In this manuscript, we extend our previous results to examine the performance of our data-assimilation approach in a variety of situations likely to be encountered when assimilating real-world observations in three-dimensional settings using surface-only observations. First, we consider the sensitivity of our data-assimilation approach to different types of parameters in an idealized setting where observations are generated from the same model used for state reconstruction (i.e. no model error). In particular, we study how a model parameter, an algorithmic parameter, and an observation parameter affect the accuracy and convergence of the algorithm. Second, we consider how the algorithm performs in the presence of model error. For these cases, we consider the effects of error in an electrophysiological parameter and in a structural parameter.

2. Methods

(a) Model

Tissue is represented using a typical monodomain formulation

$$\partial_t u = \nabla \cdot (\mathbf{D}(\mathbf{x})\nabla u) - I_{\text{ion}}, \tag{2.1}$$

where u is the voltage, $\mathbf{D}(\mathbf{x})$ is the diffusion tensor and I_{ion} is the total transmembrane ionic current. Here, the ionic current is represented by the Fenton–Karma (FK) model [19]. The FK model consists of three state variables, the voltage u and two inactivation gating variables, one for the fast inward (sodium) current and one for the slow inward (calcium) current. The model includes a third non-gated slow outward current corresponding to potassium; the three currents are summed to form I_{ion}. The parameters of the model can be tuned to set important dynamical properties including action potential duration and rate adaptation, upstroke speed, restitution curve steepness and minimum diastolic interval. It has been used previously to reproduce experimental data [19,51] and clinical data [52] as well as to reproduce the dynamics of more complicated models [19]. The FK model is used here both for the numerical prediction model within the data-assimilation algorithm and to generate truth states from which synthetic observations are created; both of these processes are described below. We use the same model parameter values as in [53]. For some cases, the excitability parameter τ_d was varied as indicated.

The domain is set in all cases to a $200 \times 200 \times 50$ grid with a spatial resolution of 0.02 cm, corresponding to a domain size of $4 \times 4 \times 1$ cm. The smallest dimension (1 cm) corresponds to the tissue thickness. No-flux boundary conditions are used on all surfaces. The model equations are solved using centred finite differencing in space and an explicit Euler method in time using a time step of 0.025 ms. The diffusion tensor $D(x)$ incorporates information about the orientation of fibres. Here, we use a simplified geometry in which fibres are oriented along a primary axis in planes parallel to the epicardial and endocardial surfaces that rotates linearly with tissue depth [19], with the total rotation 60° except when noted otherwise. Wave propagation is fastest along the fibre direction, leading to anisotropic conduction. Along the fibres, the diffusion coefficient is $0.001\,\text{cm}^2\,\text{ms}^{-1}$; in all other directions, it is $0.0002\,\text{cm}^2\,\text{ms}^{-1}$. Spiral waves were initiated using a cross-field protocol and stacked to produce a scroll wave with a transmural filament.

(b) Data assimilation

Data assimilation is the process of estimating the state of a complex system by combining a prior estimate of the system state with new observations of the system to yield a more accurate state representation. There are many methods of data assimilation, and, in fact, state estimation has been used by other groups for cardiac cells and small one-dimensional tissues [54,55] as well as two-dimensional tissue with optical mapping data [56]. Here, we build on our previous work using a variation on the ensemble Kalman filter, the local ensemble transform Kalman filter (LETKF) [57], which is particularly well suited for large three-dimensional domains.

The LETKF is one of the class of ensemble Kalman filters (EnKFs). EnKFs and variational methods, such as three-dimensional variational (3DVAR) and four-dimensional variational (4DVAR), are the two most popular classes of data-assimilation methods in use for large domains in the atmospheric and oceanic communities [58,59]. Studies have compared 4DVAR and LETKF in simple chaotic systems such as the Lorenz 40 variable model and a quasi-geostrophic atmospheric model and have found that both methods have comparable average analysis and forecast errors as long as certain analysis intervals are used [60,61]. Similar performance has also been seen in more complex models, such as with the Japanese operational atmospheric system [58]. Both ensemble Kalman filter [53,55] and variational assimilation [56,62,63] methods have been used to estimate states and conductivity parameters in cardiac tissue.

The full details of the LETKF algorithm can be found in [57] and a detailed description of the application of the LETKF to the FK model can be found in [53]. Here, we present a high-level description of the LETKF and the data assimilation process.

Data assimilation is an iterative process over time. The prior state estimate is called the background, denoted x^b, and here is given by a model simulation. The uncertainty in the background in the LETKF is assumed to be Gaussian and the covariance, $\mathbf{P}^b$, is prescribed as the sample covariance of a small number of different model simulations called the ensemble. For a collection of k ensemble members, $\{x^{b(i)} : i = 1, \ldots, k\}$, the background is the mean,

$$x^b = \frac{1}{k} \sum_{i=1}^{k} x^{b(i)},$$

with covariance

$$\mathbf{P}^b = \frac{1}{k-1} \sum_{i=1}^{k} (x^{b(i)} - x^b)\,(x^{b(i)} - x^b)^{\mathrm{T}}.$$

The background estimate and covariance are combined with the observations, y^o, and their covariance, $\mathbf{R}$, to generate the most likely state, called the analysis, x^a, and its associated covariance, $\mathbf{P}^a$. This most likely state is the one that minimizes the cost function

$$J(x) = (x - x^b)^{\mathrm{T}} \mathbf{P}^{b^{-1}} (x - x^b) + [y^o - H(x)]^T \mathbf{R}^{-1} [y^o - H(x)],$$

where $H(x)$ defines the mapping from model space to observation space. The observation covariance, $\mathbf{R}$, is taken as a constant throughout the simulation (although it does not have to be) and is prescribed as the identity matrix times the prescribed observation error. The background error covariance is never explicitly computed in the algorithm. Instead the analysis error covariance can be directly solved for in ensemble space and then the background ensemble members are transformed into the analysis ensemble through multiplication by the symmetric square root of this analysis error covariance. The new analysis is then the background plus an innovation vector based on a weighting of the difference between the observations and the background. See [57] or [53] eqns 4–6 for more details. To move to the next time, each of the analysis ensemble members is used as initial conditions for the model and integrated forward in time to the next assimilation time where the result becomes a background ensemble member at that time.

The LETKF algorithm has a few important parameters. Choices must be made about the length of the time interval between analyses as well as the size of the ensemble. The minimizing state is found at each grid point independently using only the observations that are within some prescribed radius of the grid point being estimated. This is the local piece of the LETKF and it helps both to increase the speed of the algorithm—by reducing computation and facilitating parallelization—and allows for an overall larger dimensionality of correction globally. Localizing the ensemble can also help eliminate spurious long-distance correlations that can arise due to the small ensemble size. One drawback of the ensemble Kalman filter approach is that the (likely high-dimensional) uncertainty is quantified with a relatively low-dimensional ensemble, which can lead to underestimation of the true uncertainty. One way this is addressed is by artificially inflating the ensemble covariance at every analysis step by multiplying by an inflation parameter, ρ. There are other methods of inflation, including varying the multiplicative parameter across the domain or adding some perturbation to the covariance, but in this study we elect to use a single multiplicative inflation value throughout the entire domain.

Initial values must also be selected for each of the ensemble members. This can be done by adding some type of error to the state at some time or by selecting states from a longer simulation. The advantage of selecting states from a simulation is that each of those states is physically consistent. Selecting states from a model run prior to the start of the assimilation is the approach we use here.

(c) Specific studies

In this manuscript, we perform two types of studies. First, we study the sensitivity of the data-assimilation approach to different types of parameters. There are many parameters used throughout all aspects of the data assimilation process, and it is important to quantify how the accuracy of state estimates depends on the values of these parameters. In some cases, we have expectations regarding this dependence; for example, we would expect that when tissue is thicker and other parameters remain the same, error typically would increase overall because the interior of the domain would become even further from the surface observations. Because of the large number of parameters involved, an exhaustive evaluation of all parameters is not possible. Here, we choose to study a single parameter from each of three categories: a model parameter, an algorithmic parameter and an observation parameter. Specifically, we study the effects of the total fibre rotation through the tissue depth (model parameter), the localization radius (algorithm parameter) and the standard deviation of the Gaussian error used to create synthetic observation points (observation parameter). For these cases, we will study how the accuracy of the state estimates compares as the value of each parameter of interest is varied.

Second, we analyse how the algorithm performs in the presence of model error. Here, we naturally focus on model parameters, but we choose one of each of two types of parameters, one associated with electrophysiology and one with tissue structure. The electrophysiological parameter is τ_d, which is an excitability parameter that essentially functions as the reciprocal of the sodium channel conductance. We also consider the tissue structure parameter corresponding to the total fibre rotation from the epicardial to the endocardial surface.

We emphasize that all studies in this paper are completed with synthetic observations; that is the observations are generated by subsampling a previous simulation (considered the truth) and then adding randomly generated Gaussian error with a zero mean and prescribed standard deviation. The simulation used for generating the observations is considered the 'truth' and the subsequent assimilation studies aim to estimate this known state. We note that the error is not truly Gaussian, as random errors that lead to negative voltage observations are set to zero.

To assess the accuracy of the analyses, we evaluate what percentage of the grid points are incorrectly above or below a prescribed threshold in the analysis. A point is incorrectly above the threshold if it is above the threshold in the analysis but below in the truth and incorrectly below the threshold if it is below the threshold in the analysis but above in the truth. Then we define the threshold-based error, e_{thresh}, as

$$e_{\text{thresh}} = \frac{\text{no. pts incorrectly above threshold} + \text{no. pts incorrectly below threshold}}{\text{no. points}}.$$

The magnitude of the error depends on the choice of the threshold value. Low values, being close to the fast inward (sodium) channel activation threshold (here $u_c = 0.13$), are more sensitive to noise and minor differences, so a slightly higher value is preferable to minimize such factors. However, as the threshold is increased, it becomes less meaningful because the variable u is above a high threshold for a relatively small portion of the action potential. In this paper, we use an intermediate threshold value of 0.25.

In all cases, we use an ensemble size of 20 members for the LETKF and observations that are located at every third grid point of the epicardial and endocardial surfaces of the tissue. Every third grid point corresponds to a spatial resolution of 0.06 cm. This resolution is chosen to be on the higher end of spatial resolution for optical-mapping data [64]. Observations every three grid points means that the vector y^o of observations is size $67 \times 67 \times 2 = 8978$ and the size of the background state vector x^b is $200 \times 200 \times 50 \times 3 = 6\,000\,000$, where 200, 200 and 50 are the spatial dimensions and 3 is the number of variables. The observations are taken every 5 ms, which is then the assimilation interval for all cases. All cases are initialized by using the 20 states from the previous 100 ms of the truth state. This is the method that was previously used in [53], which is also the source for the values of all remaining algorithmic parameters. As a result of the initialization method, both the initial spread and background error are large. Here, the term

spread is defined as the root mean squared distance of the ensemble members from the ensemble mean at a given point. Spread is computed pointwise at a point (x, y, z) in the domain as

$$\mathrm{sprd}(x,y,z) = \frac{1}{k-1}\left(\sum_{i=1}^{k}\left(x^{b(i)}(x,y,z) - x^{b}(x,y,z)\right)^2\right)^{1/2}.$$

(i) Sensitivity

We consider three sets of scenarios to begin exploration of the sensitivity of the data-assimilation system to changes in different parameters. Each set of scenarios uses a parameter value that was used in previous three-dimensional experiments as well as at least one different value to explore the impact of changing the parameter. The three sets of scenarios cover three different sources of sensitivity: model parameters, LETKF parameters and observation parameters.

As a model parameter, we choose the total fibre rotation. The initial scenarios studied in [53] used a fibre rotation of 60°, and here we also conduct simulations with a fibre rotation of 120°. A higher total fibre rotation while keeping the tissue thickness constant results in greater differences between the epicardial and endocardial surfaces and can lead to specific a mechanism for scroll-wave break-up as the filament accumulates localized twist [19]. Therefore, data assimilation may be more difficult for the larger twist value, as it is likely that there would be more change through the tissue that is not being observed.

For an LETKF parameter, we vary the effect of the localization radius, σ. Every observation within $2 \times \sqrt{\frac{10}{3}}\sigma$ of a grid point is used in computing the analysis at that grid point, so varying the localization radius changes which observations are used in the analysis. This is particularly important in the transmural direction as there are only observations on the epicardial and endocardial surfaces; thus, the localization radius determines how far into the tissue interior the information from the observations propagates. We use values of 4, 6, and 8 grid points. A localization radius of 6 was used in initial assimilation cases because that leads to the observations impacting the analysis close to, but not actually changing, the very centre of the tissue. A localization radius of 8 means that observations at one surface influence more than half the tissue thickness, with the centre seeing observations from both surfaces, while a radius of 4 leaves a larger gap in the centre where no change is made by the analysis.

Finally, we explore the effects of different observation errors. We previously used an observation error of 0.05 as the standard deviation of the error added to the true voltage values to obtain the synthetic data [53]. While this is a reasonable nominal error for this data, there is variability in the error experimentally and there are additional uncertainties that could increase the error such as interpolation error, representativeness error, or error caused by averaging through different tissue layers. Here, we explore the effect of doubling the observations error to 0.1 to look at the robustness of the assimilation to increased observation error.

(ii) Model error

Along with the sensitivity studies, we also consider two cases of model error, one in an electrophysiological parameter of the FK model and another in the structural parameters that define the tissue. First, we consider changes to the excitability parameter τ_d. As the value of τ_d is increased (decreased), the system becomes more (less) excitable, resulting in a steeper (less steep) action potential upstroke as well as a faster (slower) conduction velocity, among other dynamical effects. In this case, we set $\tau_d = 0.41$ in the truth state but vary its value in the numerical prediction model, including two lower values ($\tau_d = 0.39$ and $\tau_d = 0.37$) and one higher value ($\tau_d = 0.43$).

Second, because in the sensitivity studies we created synthetic observations for a fibre rotation value of 120°, we consider an additional model error experiment with error in fibre rotation. The truth is set to have fibre rotation of 120° and the corresponding observations are used, but the model used to propagate forward in time from the analysis to the next background has 60° fibre rotation.

3. Results

(a) Baseline performance

Before proceeding to the cases where parameters are varied, we first illustrate the base case of a simulation of a transmural (I-shaped) filament in a 2 cm × 2 cm × 0.5 cm domain for 1500 ms. The left column of figure 1 illustrates the truth at times spaced 500 ms apart on five parallel slices of the domain, with tissue depth in the vertical dimension stretched to improve visualization. Synthetic surface observations of the voltage variable u were made by subsampling the truth in space and time as described above. These observations were used in the data-assimilation algorithm, with the resulting updated estimate of the voltage u shown in the central column of figure 1 and the error shown in the right column. After the first assimilation, the state estimate retains its blurriness in the interior, as the influence of the surface observations does not extend throughout the entire depth; the error plot with the highest error on the interior slice also emphasizes this point. Over time, however, the state estimate improves considerably. The error remains highest in the interior of the domain and also along wavefronts and backs, but error on the surfaces essentially drops to zero and the algorithm is capable of reproducing major events like wave break-up.

For the different cases considered below, we focus on error either through the use of a time series of error plots as in the right column of figure 1 or through the use of plots of threshold error over time.

The accurate performance of the LETKF is predicated on the uncertainty in the background state being properly quantified by the spread of the ensemble. In the base case, we see that ensemble spread matches up well with the background error both in location and magnitude and, as a result, the LETKF is able to make accurate corrections and lower the overall error (figure 2). As error decreases with time, the spread also decreases, but after 1600 ms the spread is generally largest in areas where the background error is largest. The exception appears to be at the boundary of the domain on the left side of the figure, which has non-trivial background error that is not captured by the uncertainty quantification. As a result of the accuracy of the uncertainty quantification in the LETKF, the analysis threshold error is reduced over time (base case is shown as black lines in figure 3). Larger reductions in error are seen initially from the background to the analysis, which makes sense because the uncertainty is greater initially.

(b) Parameter sensitivity cases

The first scenarios we consider involve assessing the performance of the data-assimilation algorithm for different parameter regimes with no model error. In other words, we seek to assess the sensitivity of the algorithm's accuracy to different parameters. Many parameters are involved in the algorithm, so here we choose one parameter from each of three categories: model parameters, algorithmic parameters and observation parameters.

(i) Model parameter: total fibre rotation

The numerical model used by the data-assimilation algorithm includes not only the electrophysiological parameters associated with the mathematical equations (here, the 13 parameters associated with the FK model [19]) but also the parameters associated with tissue structure such as conductivity, size, and boundary conditions. Here, we consider a structural parameter consisting of the total fibre rotation across the wall. We considered cases where the true total fibre rotation $\Delta\theta$ between the epicardial and endocardial surfaces was 120° in addition to the 60° fibre rotation of the base case. The 120° rotation case is expected to be more challenging as it has the potential for greater differences between the tissue surface and the interior where there are no observations. As shown in figure 3, data assimilation does reduce the threshold error in the 120° rotation case from the background to the analysis, indicating that it is functioning properly. While the initial error reduction is similar to the 60° rotation case, the error jumps around 900–1000 ms in the 120° rotation case and stays above that of the 60° rotation error for

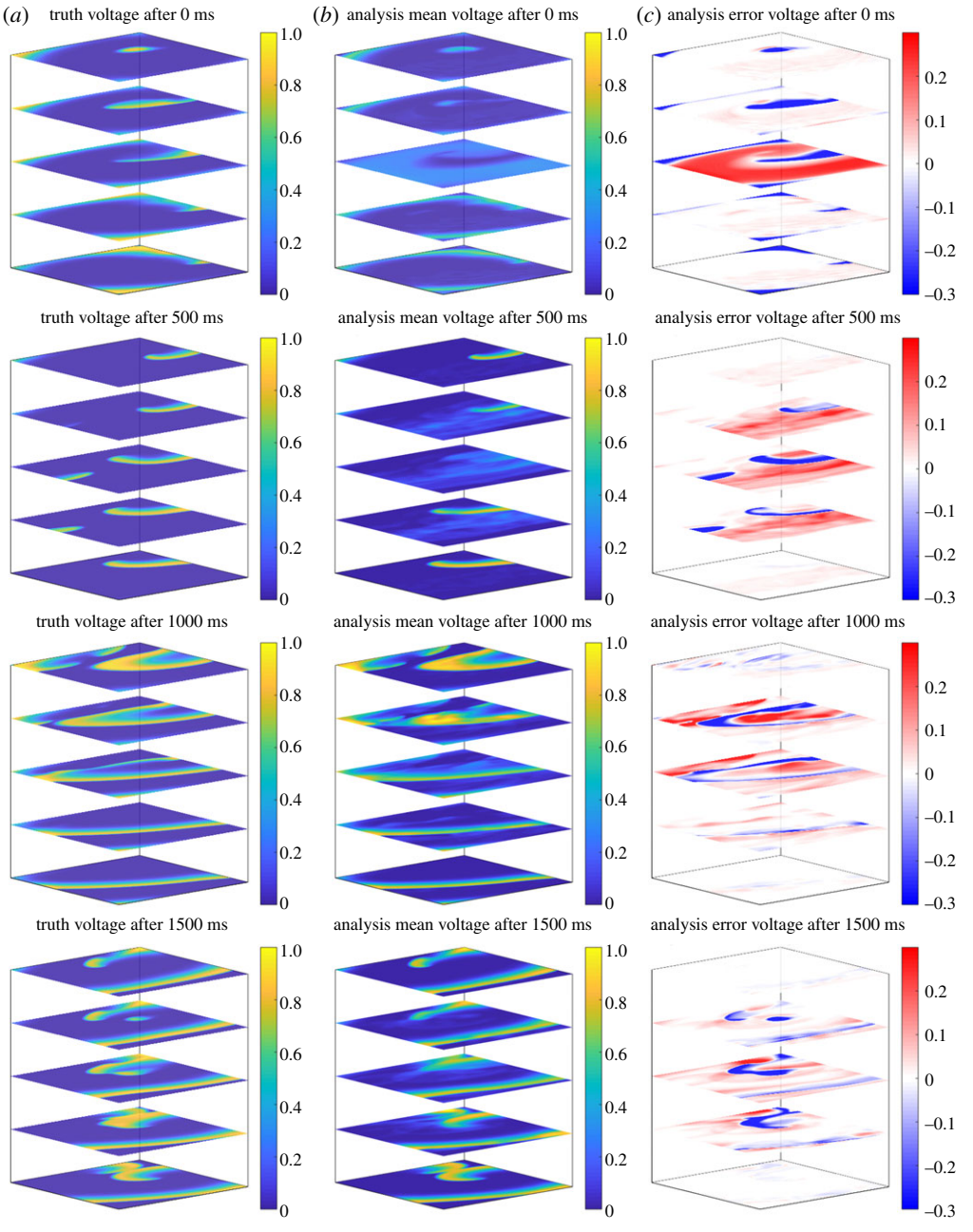

Figure 1. The truth (*a*), analysis (*b*) and analysis error (*c*) at 500 ms intervals of the baseline simulation. It is clear that the observations at the surfaces correct the surfaces quickly, but the errors are larger in the interior of the tissue. Errors are also largest along the edges of the wave. Note that the transmural direction is stretched to facilitate visualization. (Online version in colour.)

the next 500 ms. This larger error arises from the increasingly complex dynamics due to the high rate of fibre rotation [19], including increased wave breaks (many of which originate far from the surface observations) as well as faster and greater decreases in correlation between the epicardial and endocardial surfaces.

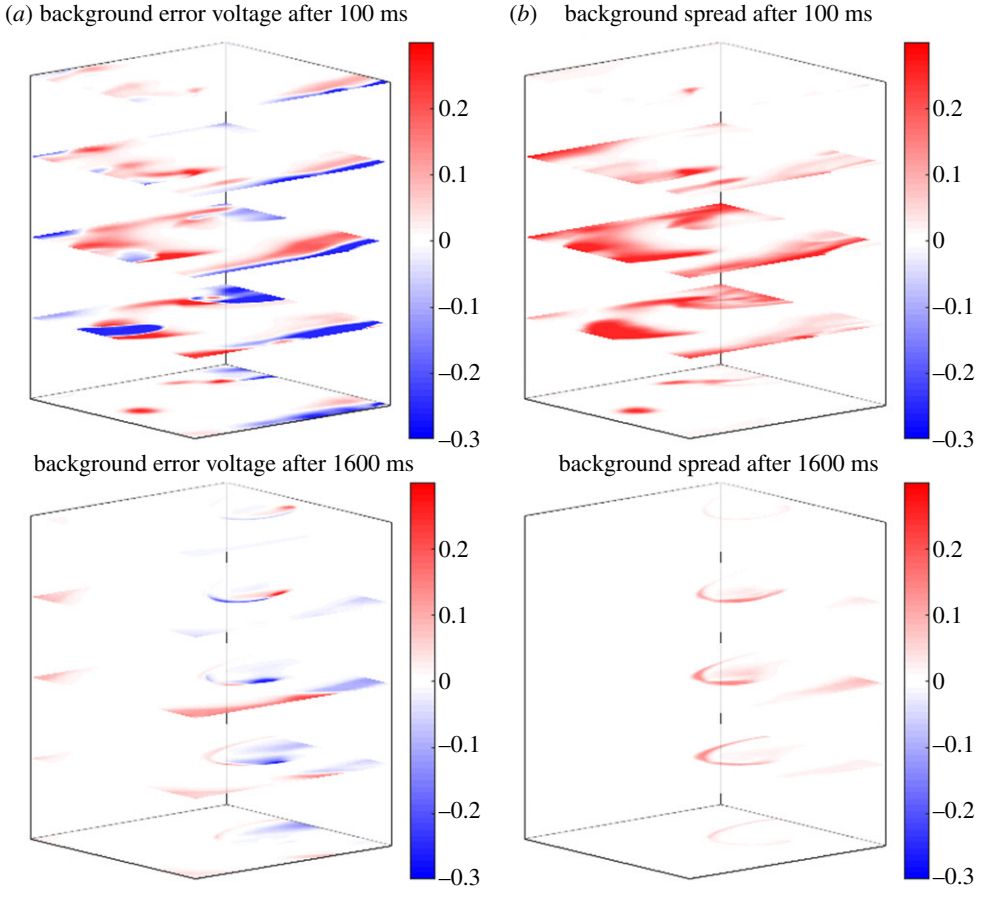

Figure 2. The background error (*a*) and the spread in the background ensemble (*b*) of the base case experiment with no model error and a total fibre rotation of 60° after 100 and 1600 ms. (Online version in colour.)

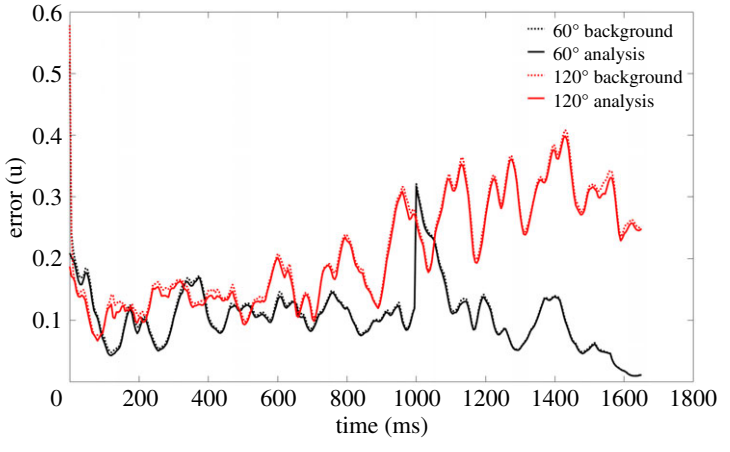

Figure 3. The threshold error of the voltage with no model error for two different total fibre rotation values: $\Delta\theta = 60^\circ$ (black) and $\Delta\theta = 120^\circ$ (red). In both cases, data assimilation reduces the error in the analysis (solid lines) from the background (dotted lines). While the 60° rotation case shows a steady reduction in error over time, the 120° rotation case has larger error after around 1000 ms. (Online version in colour.)

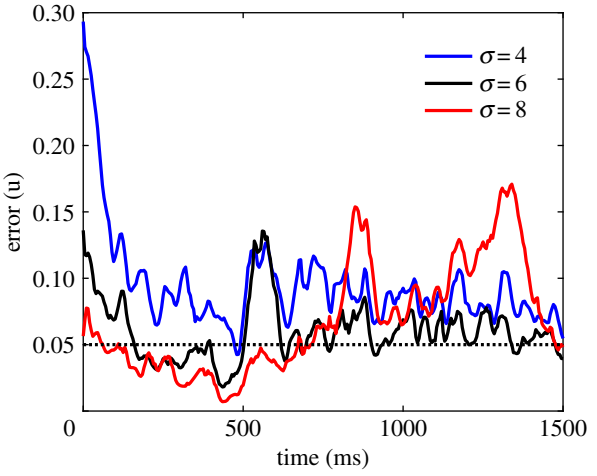

Figure 4. Error in voltage u for three values of the localization radius σ. As σ increases, each individual observation point is used to update state estimates at further distances from the location of that observation. The highest error occurs for the case with the largest value of σ, which corresponds to observations on each surface being assimilated through up to 58.4% of the tissue depth, so that the centre of the domain is influenced directly by observations on both surfaces. (Online version in colour.)

(ii) Algorithmic parameter: localization radius

The data-assimilation algorithm uses a number of different parameters, such as the ensemble size, factors to inflate the covariance matrix and the localization radius σ, which is used to identify which observations are close enough to a given grid point to include during assimilation. Here, we consider the performance of the algorithm as we set the value of σ to 4, 6 and 8, which correspond, respectively, to each individual observation point being assimilated by grid points up to 29.2, 43.8 and 58.4% of the tissue depth. The observations from both tissue surfaces can be felt in the middle of the domain thickness for $\sigma = 8$; for $\sigma = 4$ and $\sigma = 6$, the middle of the domain thickness does not use any observations during assimilation and instead is updated only indirectly.

Figure 4 shows the error in the reconstructed voltage variable obtained for the three values of σ. Initially, the scenario with $\sigma = 8$ experiences the lowest error, which suggests that the centre of the thickness benefits from assimilation of observations from both surfaces. However, over time, the dynamics of the interior may differ more significantly from the dynamics of both surfaces, which also differ from each other. Thus, the error increases for the case where $\sigma = 8$. For smaller values of σ, the error initially is large and it takes longer to decrease, as the observations provide corrections to the interior only indirectly as the dynamics change and propagate through the domain thickness. Lower error ultimately is attained when $\sigma = 6$ than when $\sigma = 4$. Therefore, σ must be chosen with care: if it is too large, the interior of the domain must merge conflicting observations, leading to larger error, whereas if it is too small, it may take too long for corrections to propagate to the interior.

(iii) Observation parameter: observation error

Because our present study uses synthetic observations to allow an assessment of accuracy, we have access to a number of parameters involved in creating these observations, including their resolution in space, time, and state variable space and the distribution used in adding noise to the subsampled truth values. Here, we consider the sensitivity to the standard deviation of the Gaussian error added to the truth values to create the synthetic observations. The base case assumed an error standard deviation of 0.05, so to investigate the impact of larger error, we test the data-assimilation algorithm while doubling the observation error standard deviation to 0.1.

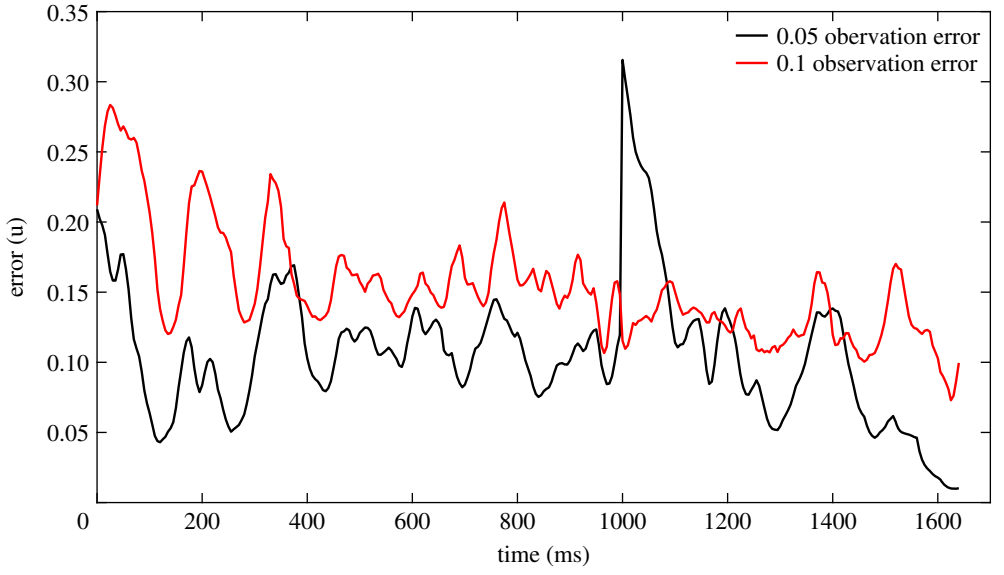

Figure 5. Threshold error in voltage u for observation error standard deviations of 0.05 (black) and 0.1 (red). As the observation error increases, the error in the analysis increases as well. (Online version in colour.)

Even with the larger error the LETKF reduces the analysis error, although the error reduction is not as swift and the analysis error using 0.1 observation error does not reach the same low levels as using 0.05 observation error (figure 5). The observation error gives a theoretical limit on the possible accuracy of the analysis, so the fact that a larger observation error leads to a large analysis error not surprising. What is encouraging is that the larger observation error does not appear to change the overall effectiveness of the LETKF in reducing the analysis error.

(c) Model error cases

In the remaining scenarios, we consider cases in which the numerical prediction model is different from the model used as the truth. Here, we consider only cases in which model parameters were changed, but it is possible to use an entirely different model for the truth (for example, we used the Beeler–Reuter for some studies in [65]) or to use experimental data for the observations.

(i) Electrophysiological parameter: excitability

To obtain some insights into the effects of varying an electrophysiological parameter, we considered the excitability τ_d, which has strong dynamical effects on conduction velocity, wavelength, and other properties. We considered one case with lowered excitability ($\tau_d = 0.43$) and two cases with higher excitability ($\tau_d = 0.39$ and $\tau_d = 0.37$) along with a reference case without model error ($\tau_d = 0.41$). The results can be seen in figure 6. For the case with no model error, the error level quickly decreases and then remains around the level of noise added to the observations. With model error, there is an asymmetry in terms of the error increases seen with increased versus decreased excitability. When the excitability is increased, higher error occurs when the value of τ_d is further from the value used in the truth, as expected. For decreased excitability, the error is higher than for either case of increased excitability. This asymmetry may be due to nonlinearity in the dynamical effects of τ_d: the system is more sensitive to decreases in excitability than to increases of the same magnitude. However, it also may stem from the corresponding effects on the data-assimilation process, in that the algorithm may find it easier to compensate for an increase in excitability than a reduction.

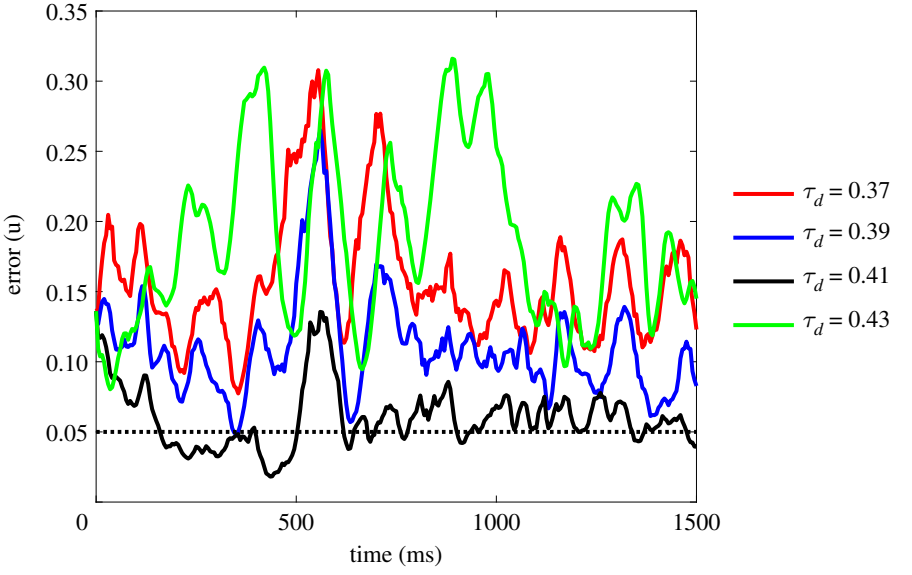

Figure 6. Error in voltage u for four values of the excitability parameter τ_d. The case with no model error ($\tau_d = 0.41$) is shown in black. The highest error occurs for the case with reduced excitability ($\tau_d = 0.43$). (Online version in colour.)

(ii) Tissue structure parameter: total fibre rotation

We also considered performance when the total fibre rotation across the myocardial wall was incorrect. Specifically, we considered two error cases to compare with the no-error case where the true total fibre rotation $\Delta\theta$ between the epicardial and endocardial surfaces was 60° and the model in the LETKF used the correct $\Delta\theta = 60°$ or 120°. In one error case, the true fibre rotation is $\Delta\theta = 60^o$ while the model has the incorrect 120° fibre rotation and in the other the true fibre rotation is $\Delta\theta = 120°$ and the model in the LETKF has a fibre rotation of 60°. In other words, in the base case this is the same fibre rotation as in the truth from which the observations are sampled, whereas in the other cases, the observations come from truth simulations using total fibre rotations that are different than the model used in the LEKTF.

In all three cases, the error is immediately reduced to around 0.1 owing to the incorporation of observations (figure 7). The model-error and no-model-error cases have similar error for approximately the first 1000 ms. After around 1000 ms, the case with no model error continues to reduce error, while error increases when the LETKF uses incorrect fibre rotation in the model for the ensemble forecast. Both cases with fibre rotation error exhibit similar error patterns.

The fact that the state is initially well approximated even with the model error indicates that data assimilation has the potential to correct for model error. One potential reason for the eventual divergence could be that because each ensemble member uses the same incorrect model, the model error is not represented in the spread and thus the system develops too much confidence in the forecasts. The global root mean squared spread in the model-error case continues to decrease over time, even as the error begins to increase after 1000 ms, as shown in figure 8.

The ensemble spread is supposed to quantify the uncertainty in the state estimate, but because the same model is used to propagate each ensemble member, the background ensemble is mostly quantifying dynamic uncertainty in the system and not any model-driven uncertainty. Soon after the start of the assimilation, the uncertainty and the error near the epicardial and endocardial surfaces are low because the initial large uncertainty allows the LETKF to fit its state estimate closely to the data available at the surfaces; see top row of figure 9. Over time, the ensemble members begin to converge and make similar incorrect forecasts for the epicardial and endocardial surfaces. However, because the ensemble spread is low, the LETKF incorrectly

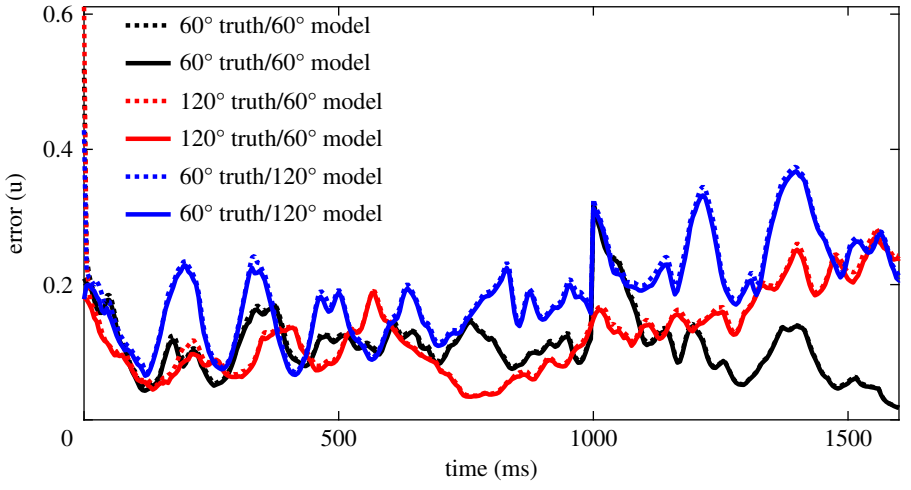

Figure 7. Error in voltage *u* in the case where there is model error in the total fibre rotation. The threshold error can be seen for the base case when the truth has 60° fibre rotation along with the model used in the data assimilation (black). There are two error cases, one where the truth has 120° and the model has 60° (red) fibre rotation and the opposite case where the truth has 60° and the model has 120° (blue) fibre rotation. Similar improvement is seen initially in all cases, but the model error begins to cause increased error after 800–1000 ms. (Online version in colour.)

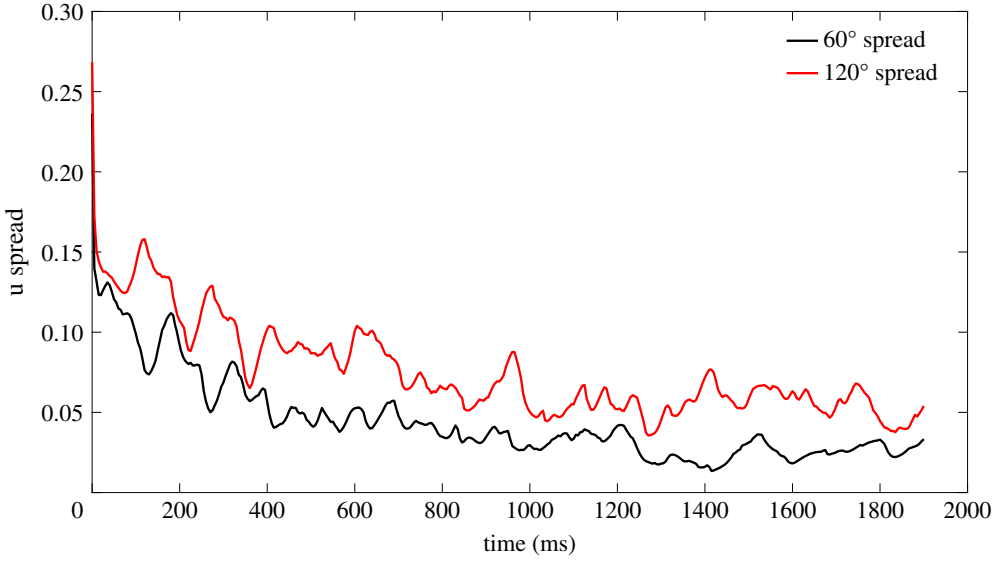

Figure 8. The global root mean squared spread in the background ensemble in the LETKF when there is no model error and the truth has 60° total fibre rotation (black) and when there is model error and the truth has 120° fibre rotation (red). The spread decreases in both cases, which indicates the LETKF believes the uncertainty is reduced in both cases. In the model error case, however, the error is actually growing, as seen in figure 7. (Online version in colour.)

believes that these forecasts are accurate, even though the actual background error at the epicardial and endocardial surfaces is high (figure 9, bottom row). As a result, only very small corrections are made, even though the error is large and observations are available at the surface locations.

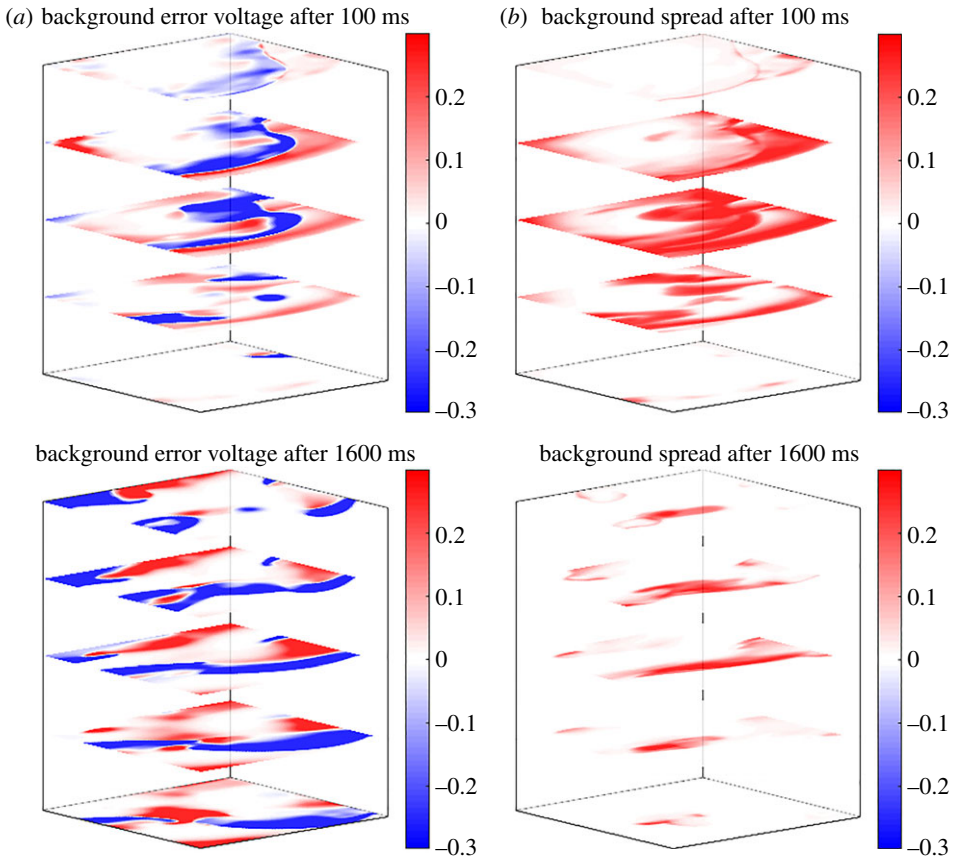

Figure 9. The background error (*a*) and the spread in the background ensemble (*b*) of the scenario with model error in the total fibre rotation of 120° rotation in the truth but 60° rotation in the model used for the ensemble forecast) after 100 and 1600 ms. (Online version in colour.)

4. Discussion

In this paper, we have studied the performance of an LETKF-based data-assimilation algorithm at reconstructing three-dimensional cardiac scroll wave states as different parameters were varied. Specifically, we considered how performance depended on different ranges of model, algorithmic and observation parameters and on the presence of model error through electrophysiological and structural parameters.

Overall, the performance of the LETKF was fairly robust to parameter changes as none of the scenarios here saw the assimilation fail. In particular, in both observation error cases, the same trend is seem in which the limiting value of the error (without model error) depends linearly on the magnitude of the observation error. Variations in the localization parameter indicated the need to choose an intermediate value, as the localization radius of $\sigma = 6$ had the lowest error of the localization parameters. This choice allowed surface observations to be felt over a long distance while also ensuring they would not influence assimilation directly beyond the centre of the domain to avoid difficulties with merging potentially conflicting observations.

Error was larger in the other cases, most notably when the fibre rotation was increased to 120° in both the sensitivity and model-error cases. Errors in the model led to systematic errors in the assimilation results because the background ensemble spread decreases and no longer accurately quantifies the uncertainty of the system. Even so, there was initial error reduction in the model-error cases even if there is potential for drift away from the true solution as time passes. An

important future goal will be to identify ways to prevent the ensemble from collapsing in this manner. In our previous one-dimensional studies [65], we used additive error to increase the spread of the ensemble. With additive error, perturbations are addition to ensemble members with the goal of introducing new directions to the ensemble. Previously, we added a multiple of the difference in the state at a randomly selected time and the state one assimilation interval (5 ms) later in a prior run of the model. An additional benefit was that after incorporating additive inflation, performance was similar regardless of the chosen multiplicative inflation parameter, thereby improving the robustness of the algorithm and reducing the need for fine-tuning. Another possibility we have not yet pursued would be better representing model error into the ensemble framework through a parameter ensemble or a multi-model system [66,67].

(a) Connections to uncertainty quantification

Data assimilation inherently involves reconciling model predictions with experimental data, which is at the heart of efforts to quantify uncertainty in models. Within this manuscript, we have focused on using data assimilation for state reconstruction, but it can be used in other ways that complement ongoing work in uncertainty quantification (UQ) for cardiac models. UQ in the framework of ensemble Kalman filter data assimilation is accomplished through the ensemble.

One important way in which data assimilation can be extended is to estimate parameters; global parameters can be added to an augmented state vector and their time derivatives set to zero, so that their values will receive updates when the state is corrected. Some preliminary efforts in this direction are given in [68], which found in a one-dimensional setting that some, but not all, FK parameters could be estimated accurately and reliably in this manner. Another possibility to consider in the future would be to identify robust interpretations in the context of UQ of the measures of uncertainty associated with the ensemble. In the standard LETKF framework, it is assumed that the largest source of uncertainty is due to the system dynamics. In parameter estimation or dealing with other types of model error, using a multi-model approach can help to incorporate uncertainty associated with different model parameters into the ensemble. Care must be taken, however, to ensure that the ensemble size does not dramatically increase and slow down the computation. There may be parallels with population-based approaches currently in use by the broader modelling community [43–48], especially if the ensemble members use different parameter values.

(b) Limitations

Our work involves a number of important limitations. We necessarily limited our studies to a small number of parameters. We may see differences in results when studying more values of the parameters or when considering the effects of other parameters. The data-assimilation algorithm includes randomness in the generation of synthetic observations, but we did not make comparisons of different observation sets; in addition, we considered only single cases of dynamical states and ensemble initialization. Most of the simulations were run for 1.5-2 s. Although this is enough time for complex dynamics to develop, it is possible that the data-assimilation performance may be affected over longer runs either positively (through improved state reconstruction with time) or negatively (through the occurrence of ensemble collapse, when the individual ensemble members converge and the resulting overconfidence in the numerical prediction leads to a downplaying of the observations). For the FK model used for numerical prediction, we used a single set of parameter values with the intention of achieving a sustained spiral-wave break-up scenario. Different parameters for the model, such as more realistic values of τ_d corresponding to higher excitability, may lead to different results. In particular, differences in dynamical states (e.g. more or more complex spiral-wave break-up) may lead to differences in performance. Although we studied many of these types of variations previously in one-dimensional rings [65], we cannot guarantee similar results will occur in three-dimensional cases.

A minor limitation of our current implementation is that the localization radius is uniform in all three dimensions. Although we expect that the performance effects when varying the localization radius are dominated by the differences in the depth of observations included when assimilating each grid point, it is possible that the number of observations included in the other directions may have secondary effects. A localization procedure with a different radius for the transmural direction, or even an anisotropic localization taking fibre orientation into account, could show some differences in results.

(c) Future work

Our next steps include implementing additive inflation for three-dimensional cases and considering the use of different parameter values or even models in the ensemble with the goal of reducing the incidence of ensemble collapse. We also would like to study algorithm performance over a broader range of dynamical states and using observations obtained from experiments rather than synthetic observations. In addition, we wish to analyse in more detail the effects of observation spatial distribution on the results as a function of tissue thickness and dynamics, with the goal of determining the applicability of our approach to the clinical setting.

Data accessibility. This article has no additional data.

Authors' contributions. Both authors contributed equally in all aspects of preparing this paper.

Competing interests. We declare we have no competing interest.

Funding. This work was supported in part by the National Science Foundation under grant no. CMMI-1762803.

Acknowledgements. This work used the Extreme Science and Engineering Discovery Environment (XSEDE) comet at the San Diego Supercomputing Center through allocation TG-IBN050000N.

References

1. Davidenko JM, Pertsov AV, Salomonsz R, Baxter W, Jalife J. 1992 Stationary and drifting spiral waves of excitation in isolated cardiac muscle. *Nature* **355**, 349–351. (doi:10.1038/355349a0)
2. Gray RA, Pertsov AM, Jalife J. 1998 Spatial and temporal organization during cardiac fibrillation. *Nature* **392**, 75–78. (doi:10.1038/32164)
3. Witkowski FX, Leon LJ, Penkoske PA, Giles WR, Spano ML, Ditto WL, Winfree AT. 1998 Spatiotemporal evolution of ventricular fibrillation. *Nature* **392**, 78–82. (doi:10.1038/32170)
4. Choi BR, Salama G. 2000 Simultaneous maps of optical action potentials and calcium transients in guinea-pig hearts: mechanisms underlying concordant alternans. *J. Physiol. (Lond.)* **529**, 171–188. (doi:10.1111/j.1469-7793.2000.00171.x)
5. Salama G. 2001 Optical Mapping: Background and Historial Perspective. In *Optical mapping of cardiac excitation and arrhythmias* (eds DS Rosenbaum, J Jalife), pp. 9–31. Armonk, NY: Futura Publishing Co.
6. Efimov IR, Nikolski VP, Salama G. 2004 Optical imaging of the heart. *Circ. Res.* **95**, 21–33. (doi:10.1161/01.RES.0000130529.18016.35)
7. Uzelac I, Ji YC, Hornung D, Schröder-Scheteling J, Luther S, Gray RA, Cherry EM, Fenton FH. 2017 Simultaneous quantification of spatially discordant alternans in voltage and intracellular calcium in langendorff-perfused rabbit hearts and inconsistencies with models of cardiac action potentials and Ca transients. *Front. Physiol.* **8**, 819. (doi:10.3389/fphys.2017.00819)
8. Walton RD, Bernus O. 2015 Towards depth-resolved optical imaging of cardiac electrical activity. *Adv. Exp. Med. Biol.* **859**, 405–423. (doi:10.1007/978-3-319-17641-3_16)
9. Guevara MR, Ward G, Shrier A, Glass L. 1984 Electrical alternans and period-doubling bifurcations. *Comput. Cardiol.* **11**, 167–170.
10. Karma A. 1994 Electrical alternans and spiral wave breakup in cardiac tissue. *Chaos* **4**, 461–472. (doi:10.1063/1.166024)
11. Qu Z, Garfinkel A, Chen PS, Weiss JN. 2000 Mechanisms of discordant alternans and induction of reentry in simulated cardiac tissue. *Circulation* **102**, 1664–1670. (doi:10.1161/01.CIR.102.14.1664)
12. Watanabe MA, Fenton FH, Evans SJ, Hastings HM, Karma A. 2001 Mechanisms for discordant alternans. *J. Cardiovasc. Electrophysiol.* **12**, 196–206. (doi:10.1046/j.1540-8167.2001.00196.x)

13. Shiferaw Y, Watanabe MA, Garfinkel A, Weiss JN, .Karma A. 2003 Model of intracellular calcium cycling in ventricular myocytes. *Biophys. J.* **85**, 3666–3686. (doi:10.1016/S0006-3495(03)74784-5)
14. Cherry EM, Fenton FH. 2004 Suppression of alternans and conduction blocks despite steep APD restitution: electrotonic, memory, and conduction velocity restitution effects. *Am. J. Physiol. Heart Circ. Physiol.* **286**, H2332–H2341. (doi:10.1152/ajpheart.00747.2003)
15. Restrepo JG, Karma A. 2009 Spatiotemporal intracellular calcium dynamics during cardiac alternans. *Chaos* **19**, 037115. (doi:10.1063/1.3207835)
16. Sato D, Bers DM, Shiferaw Y. 2013 Formation of spatially discordant alternans due to fluctuations and diffusion of calcium. *PLoS ONE* **8**, e85365. (doi:10.1371/journal.pone.0085365)
17. Chen DD, Gray RA, Uzelac I, Herndon C, Fenton FH. 2017 Mechanism for amplitude alternans in electrocardiograms and the initiation of spatiotemporal chaos. *Phys. Rev. Lett.* **118**, 168101. (doi:10.1103/PhysRevLett.118.168101)
18. Biktashev VN, Holden AV, Zhang H. 1994 Tension of organizing filaments of scroll waves. *Phil. Trans. R. Soc. Lond. A* **347**, 611–630. (doi:10.1098/rsta.1994.0070)
19. Fenton F, Karma A. 1998 Vortex dynamics in three-dimensional continuous myocardium with fiber rotation: filament instability and fibrillation. *Chaos* **8**, 20–47. (doi:10.1063/1.166311)
20. Qu Z, Kil J, Xie F, Garfinkel A, Weiss JN. 2000 Scroll wave dynamics in a three-dimensional cardiac tissue model: roles of restitution, thickness, and fiber rotation. *Biophys. J.* **78**, 2761–2775. (doi:10.1016/S0006-3495(00)76821-4)
21. Rappel W-J. 2001 Filament instability and rotational tissue anisotropy: a numerical study using detailed cardiac models. *Chaos* **11**, 71–80. (doi:10.1063/1.1338128)
22. Fenton FH, Cherry EM, Hastings HM, Evans SJ. 2002 Multiple mechanisms of spiral wave breakup in a model of cardiac electrical activity. *Chaos* **12**, 852–892. (doi:10.1063/1.1504242)
23. Clayton RH. 2008 Vortex filament dynamics in computational models of ventricular fibrillation in the heart. *Chaos* **18**, 043127. (doi:10.1063/1.3043805)
24. ten Tusscher KHWJ, Mourad A, Nash MP, Clayton RH, Bradley CP, Paterson DJ, Hren R, Hayward M, Panfilov AV, Taggart P. 2009 Organization of ventricular fibrillation in the human heart: experiments and models. *Exp. Physiol.* **94**, 553–562. (doi:10.1113/expphysiol.2008.044065)
25. Rappel WJ, Fenton F, Karma A. 1999 Spatiotemporal control of wave instabilities in cardiac tissue. *Phys. Rev. Lett.* **83**, 456–459. (doi:10.1103/PhysRevLett.83.456)
26. Echebarria B, Karma A. 2002 Spatiotemporal control of cardiac alternans. *Chaos* **12**, 923–930. (doi:10.1063/1.1501544)
27. Krogh-Madsen T, Karma A, Riccio ML, Jordan PN, Christini DJ, Gilmour RF. 2010 Off-site control of repolarization alternans in cardiac fibers. *Phys. Rev. E Stat. Nonlin. Soft Matter Phys.* **81**, 011915. (doi:10.1103/PhysRevE.81.011915)
28. Muñoz LM, Stockton JF, Otani NF. 2010 Applications of control theory to the dynamics and propagation of cardiac action potentials. *Ann. Biomed. Eng.* **38**, 2865–2876. (doi:10.1007/s10439-010-0037-z)
29. Garzón A, Grigoriev RO, Fenton FH. 2011 Model-based control of cardiac alternans in Purkinje fibers. *Phys. Rev. E* **84**, 041927. (doi:10.1103/PhysRevE.84.041927)
30. Garzón A, Grigoriev RO, Fenton FH. 2014 Continuous-time control of alternans in long Purkinje fibers. *Chaos* **24**, 033124. (doi:10.1063/1.4893295)
31. Cherry EM. 2017 Distinguishing mechanisms for alternans in cardiac cells using constant-diastolic-interval pacing. *Chaos* **27**, 093902. (doi:10.1063/1.4999354)
32. Ji YC, Uzelac I, Otani N, Luther S, Gilmour RF, Cherry EM, Fenton FH. 2017 Synchronization as a mechanism for low-energy anti-fibrillation pacing. *Heart Rhythm* **14**, 1254–1262. (doi:10.1016/j.hrthm.2017.05.021)
33. Zlochiver S, Johnson C, Tolkacheva EG. 2017 Constant DI pacing suppresses cardiac alternans formation in numerical cable models. *Chaos* **27**, 093903. (doi:10.1063/1.4999355)
34. Syed Z, Vigmond E, Nattel S, Leon LJ. 2005 Atrial cell action potential parameter fitting using genetic algorithms. *Med. Biol. Eng. Comput.* **43**, 561–571. (doi:10.1007/BF02351029)
35. Bot CT, Kherlopian AR, Ortega FA, Christini DJ, Krogh-Madsen T. 2012 Rapid genetic algorithm optimization of a mouse computational model: benefits for anthropomorphization of neonatal mouse cardiomyocytes. *Front. Physiol.* **3**, 421. (doi:10.3389/fphys.2012.00421)

36. Groenendaal W, Ortega FA, Kherlopian AR, Zygmunt AC, Krogh-Madsen T, Christini DJ. 2015 Cell-specific cardiac electrophysiology models. *PLoS Comput. Biol.* **11**, e1004242. (doi:10.1371/journal.pcbi.1004242)
37. Cairns DI, Fenton FH, Cherry EM. 2017 Efficient parameterization of cardiac action potential models using a genetic algorithm. *Chaos* **27**, 093922. (doi:10.1063/1.5000354)
38. Coveney S, Clayton RH. 2018 Fitting two human atrial cell models to experimental data using Bayesian history matching. *Prog. Biophys. Mol. Biol.* **139**, 43–58. (doi:10.1016/j.pbiomolbio.2018.08.001)
39. Mitchell CC, Schaeffer DG. 2003 A two-current model for the dynamics of cardiac membrane. *Bull. Math. Biol.* **65**, 767–793. (doi:10.1016/S0092-8240(03)00041-7)
40. Bueno-Orovio A, Cherry EM, Fenton FH. 2008 Minimal model for human ventricular action potentials in tissue. *J. Theor. Biol.* **253**, 544–560. (doi:10.1016/j.jtbi.2008.03.029)
41. Corrado C, Niederer SA. 2016 A two-variable model robust to pacemaker behaviour for the dynamics of the cardiac action potential. *Math. Biosci.* **281**, 46–54. (doi:10.1016/j.mbs.2016.08.010)
42. Dokos S, Lovell NH. 2004 Parameter estimation in cardiac ionic models. *Prog. Biophys. Mol. Biol.* **85**, 407–431. (doi:10.1016/j.pbiomolbio.2004.02.002)
43. Sarkar AX, Christini DJ, Sobie EA. 2012 Exploiting mathematical models to illuminate electrophysiological variability between individuals. *J. Physiol. (Lond.)* **590**, 2555–2567. (doi:10.1113/jphysiol.2011.223313)
44. Britton OJ, Bueno-Orovio A, Van Ammel K, Lu HR, Towart R, Gallacher DJ, Rodriguez B. 2013 Experimentally calibrated population of models predicts and explains intersubject variability in cardiac cellular electrophysiology. *Proc. Natl Acad. Sci. USA* **110**, E2098–E2105. (doi:10.1073/pnas.1304382110)
45. Sánchez C, Bueno-Orovio A, Wettwer E, Loose S, Simon J, Ravens U, Pueyo E, Rodriguez B. 2014 Inter-subject variability in human atrial action potential in sinus rhythm versus chronic atrial fibrillation. *PLoS ONE* **9**, e105897. (doi:10.1371/journal.pone.0105897)
46. Liberos A, Bueno-Orovio A, Rodrigo M, Ravens U, Hernandez-Romero I, Fernandez-Aviles F, Guillem MS, Rodriguez B, Climent AM. 2016 Balance between sodium and calcium currents underlying chronic atrial fibrillation termination: an in silico intersubject variability study. *Heart Rhythm* **13**, 2358–2365. (doi:10.1016/j.hrthm.2016.08.028)
47. Devenyi RA, Ortega FA, Krogh-Madsen T, Christini DJ, Sobie EA. 2016 Population-based mathematical modeling facilitates the interpretation of dynamic clamp experiments in cardiomyocytes. *Biophys. J.* **110**, 585a. (doi:10.1016/j.bpj.2015.11.3125)
48. Gemmell P, Burrage K, Rodríguez B, Quinn TA. 2016 Rabbit-specific computational modelling of ventricular cell electrophysiology: using populations of models to explore variability in the response to ischemia. *Prog. Biophys. Mol. Biol.* **121**, 169–184. (doi:10.1016/j.pbiomolbio.2016.06.003)
49. Pathmanathan P, Shotwell MS, Gavaghan DJ, Cordeiro JM, Gray RA. 2015 Uncertainty quantification of fast sodium current steady-state inactivation for multi-scale models of cardiac electrophysiology. *Prog. Biophys. Mol. Biol.* **117**, 4–18. (doi:10.1016/j.pbiomolbio.2015.01.008)
50. Mirams GR, Pathmanathan P, Gray RA, Challenor P, Clayton RH. 2016 Uncertainty and variability in computational and mathematical models of cardiac physiology. *J. Physiol. (Lond.)* **594**, 6833–6847. (doi:10.1113/JP271671)
51. Oliver RA, Krassowska W. 2005 Reproducing cardiac restitution properties using the Fenton-Karma membrane model. *Ann. Biomed. Eng.* **33**, 907–911. (doi:10.1007/s10439-005-3948-3)
52. Lombardo DM, Fenton FH, Narayan SM, Rappel W-J. 2016 Comparison of detailed and simplified models of human atrial myocytes to recapitulate patient specific properties. *PLoS Comput. Biol.* **12**, e1005060. (doi:10.1371/journal.pcbi.1005060)
53. Hoffman MJ, LaVigne NS, Scorse ST, Fenton FH, Cherry EM. 2016 Reconstructing three-dimensional reentrant cardiac electrical wave dynamics using data assimilation. *Chaos* **26**, 013107. (doi:10.1063/1.4940238)
54. Muñoz LM, Otani NF. 2010 Enhanced computer modeling of cardiac action potential dynamics using experimental data-based feedback. *Comput. Cardiol.* **37**, 837–840.
55. Muñoz LM, Otani NF. 2013 Kalman filter based estimation of ionic concentrations and gating variables in a cardiac myocyte model. *Comput. Cardiol.* **40**, 53–56.

56. Barone A, Gizzi A, Fenton F, Filippi S, Veneziani A. 2020 Experimental validation of a variational data assimilation procedure for estimating space-dependent cardiac conductivities. *Comput. Methods Appl. Mech. Eng.* **358**, 112615. (doi:10.1016/j.cma.2019.112615)
57. Hunt BR, Kostelich EJ, Szunyogh I. 2007 Efficient data assimilation for spatiotemporal chaos: a local ensemble transform Kalman filter. *Physica D* **230**, 112–126. (doi:10.1016/j.physd.2006.11.008)
58. Miyoshi T, Sato Y, Kadowaki T. 2010 Ensemble Kalman filter and 4D-var intercomparison with the japanese operational global analysis and prediction system. *Mon. Weather Rev.* **138**, 2846–2866. (doi:10.1175/2010MWR3209.1)
59. Hoffman MJ, Miyoshi T, Haine T, Ide K, Murtugudde R, Brown CW. 2012 An advanced data assimilation system for the Chesapeake Bay. *J. Atmos. Oceanic Tech.* **29**, 1542–1557. (doi:10.1175/JTECH-D-11-00126.1)
60. Fertig EJ, Harlim J, Hunt BR. 2007 A comparative study of 4D-VAR and a 4D Ensemble Kalman Filter: perfect model simulations with Lorenz-96. *Tellus A* **59**, 96–100. (doi:10.1111/j.1600-0870.2006.00205.x)
61. Yang S-C, Corazza M, Carrassi A, Kalnay E, Miyoshi T. 2009 Comparison of local ensemble transform Kalman filter, 3DVAR, and 4DVAR in a quasigeostrophic model. *Monthly Weather Rev.* **137**, 693–709. (doi:10.1175/2008MWR2396.1)
62. Yang H, Veneziani A. 2015 Estimation of cardiac conductivities in ventricular tissue by a variational approach. *Inverse Prob.* **31**, 115001. (doi:10.1088/0266-5611/31/11/115001)
63. Graham LS, Kilpatrick D. 2010 Estimation of the bidomain conductivity parameters of cardiac tissue from extracellular potential distributions initiated by point stimulation. *Ann. Biomed. Eng.* **38**, 3630–3648. (doi:10.1007/s10439-010-0119-y)
64. Gizzi A, Cherry E, Gilmour R, Luther S, Filippi S, Fenton F. 2013 Effects of pacing site and stimulation history on alternans dynamics and the development of complex spatiotemporal patterns in cardiac tissue. *Front. Physiol.* **4**, 71. (doi:10.3389/fphys.2013.00071)
65. LaVigne NS, Holt N, Hoffman MJ, Cherry EM. 2017 Effects of model error on cardiac electrical wave state reconstruction using data assimilation. *Chaos* **27**, 093911. (doi:10.1063/1.4999603)
66. Dillon ME, Skabar YG, Ruiz J, Kalnay E, Collini EA, Echevarría P, Saucedo M, Miyoshi T, Kunii M. 2016 Application of the WRF-LETKF data assimilation system over southern South America: sensitivity to model physics. *Weather Forecast.* **31**, 217–236. (doi:10.1175/WAF-D-14-00157.1)
67. Krishnamurti TN, Kishtawal CM, Zhang Z, LaRow T, Bachiochi D, Williford E, Gadgil S, Surendran S. 2000 Multimodel ensemble forecasts for weather and seasonal climate. *J. Clim.* **13**, 4196–4216. (doi:10.1175/1520-0442(2000)013<4196:MEFFWA>2.0.CO;2)
68. Holt N. 2019 Parameter estimation of a cardiac model using the local ensemble transform Kalman filter. Master's thesis, Rochester Institute of Technology, Rochester, NY.